Mon. Not. R. Astron. Soc. **000**, 000–000 (0000) Printed 30 September 2009 (MN LATEX style file v2.2)

Measuring mass-loss rates and constraining shock physics for ten OB stars using *Chandra* X-ray emission line profiles

Emma E. Wollman,[1] David H. Cohen,[1] Maurice A. Leutenegger,[2]
Stanley P. Owocki,[3] Janos Zsargó,[4] D. John Hillier[4]
[1] *Swarthmore College, Department of Physics and Astronomy, Swarthmore, Pennsylvania 19081, USA*
[2] *NASA/Goddard Space Flight Center, Laboratory for High Energy Astrophysics, Code 622, Greenbelt, Maryland 20771, USA*
[3] *University of Delaware, Bartol Research Institute, Newark, Delaware 19716, USA*
[4] *University of Pittsburgh, Department of Physics and Astronomy, 3941 O'Hara St., Pittsburgh, Pennsylvania 15260, USA*

30 September 2009

ABSTRACT
X-ray spectral lines provide a powerful diagnostic of massive star winds. An X-ray emission line's characteristic shape is affected by the kinematics of the hot plasma where the X-rays are produced and by the properties of the attenuating bulk material of the wind, so X-rays can be used as a probe of both wind components. Qualitatively, X-ray lines in massive stars have been observed to lack the signatures of absorption that are predicted by other diagnostics. In this paper, following the methods of Cohen et al. (2009), we analyze the spectra of ten stars from the *Chandra* archive in order to 1) quantify the amount of absorption by determining mass-loss rates for all stars and 2) test predictions of the wind-shock X-ray production scenario by determining onset radii and terminal velocities for the X-ray producing material. We obtain mass-loss rate reductions of between a factor of 3 and an order of magnitude, and find that our results are in general agreement with the predictions of the wind-shock model.

Key words: stars: mass-loss – stars: winds, outflows – X-rays: stars

1 INTRODUCTION

By losing mass at a rate of about 10^{-6} $M_\odot$ yr^{-1} via its stellar wind, an O star can shed a significant portion of its mass over the course of its lifetime. This continuous loss of mass transfers energy and momentum to the surrounding interstellar medium, and so the mass-loss rate is an important parameter in the study of both stellar evolution and of the galactic interstellar medium.

In this paper we apply a new method of mass-loss rate determination based on the analysis of X-ray emission line profiles (Cohen et al. 2009) to the *Chandra* grating spectra of ten massive stars. The characteristic profile shape arises because red-shifted photons emitted from the rear hemisphere of the wind are subject to more attenuation than the blue-shifted photons originating in the front hemisphere (see figure 2 in Cohen et al. (2009)). The degree of blue shift and asymmetry in these line profiles is then directly proportional to the wind column density and thus to the mass-loss rate. By fitting a simple quantitative model (Owocki & Cohen 2001) to each emission line in a star's spectrum and then analyzing the ensemble of lines, we can robustly determine the star's mass-loss rate.

Because this diagnostic scales with the column density rather than the square of the density, it avoids many of the problems presented by traditional mass-loss rate diagnostics. In particular, density-squared diagnostics such as Hα and radio or IR free-free emission will overestimate the mass-loss rate if clumping is not accounted for. UV absorption line diagnostics are sensitive to ionization corrections which are highly uncertain and also are subject to density-squared clumping effects. Recent, more sophisticated application of these diagnostics has led to a downward revision of mass-loss rates of O stars (Bouret et al. 2005; Fullerton et al. 2006; Puls et al. 2006). These lowered mass-loss rates provide a natural explanation for the initially surprising discovery (Kahn et al. 2001; Cassinelli et al. 2001) that X-ray profiles are not as symmetric as traditional mass-loss rate estimates had implied.

The initial application of our X-ray line profile based mass-loss rate diagnostic to the O supergiant ζ Pup gave a mass-loss rate of 3.5×10^{-6} $M_\odot$ yr^{-1} (Cohen et al. 2009). This represents a factor of three reduction over the traditional estimate that does not account for clumping, and is consistent with a newer analysis of the Hα and radio data which produces an upper limit of $\dot{M} = 4.2 \times 10^{-6}$ $M_\odot$ yr^{-1} when the effects of clumping are accounted for (Puls et al. 2006). While small-scale clumping reconciles the X-ray, UV, and radio data for ζ Pup, there is no direct evidence for large-scale clumping, or porosity, in the X-ray data them-

selves (Cohen et al. 2008). Porosity results from optically thick clumps, which can "hide" opacity in their interiors. While porosity has been proposed as an explanation for the more-symmetric-than-expected X-ray line profiles (Oskinova et al. 2006), very large porosity lengths are required in order for porosity to have any effect on line profiles (Owocki & Cohen 2006). In this paper, we derive mass-loss rates from the measured X-ray line profiles under the assumption that significant porosity is not present.

An additional goal of this paper is to constrain wind-shock models of X-ray production by extracting kinematic information from the line profiles. The profiles are Doppler broadened by the bulk motion of the hot plasma embedded in the highly supersonic wind. Our quantitative line-profile model allows us to derive an onset radius of shock-heated plasma and also, for the highest signal-to-noise lines, the terminal velocity of the X-ray emitting plasma. We use these quantities to test the predictions of numerical simulations of wind-shock X-ray production.

The paper is organized as follows: In the next section we describe the data and our sample of OB stars taken from the *Chandra* archive. In §3 we describe our data analysis and modeling methodology including the line profile model, which was first introduced by Owocki & Cohen (2001), the line-profile fitting procedure, and the derivation of the mass-loss rate from an ensemble of line fits. In §4 we present our results, including mass-loss rate determinations for each star in our sample, and in §5 we conclude with a discussion of the implications of the line profile fitting results.

2 THE PROGRAM STARS

2.1 Observations

All observations were made with *Chandra*'s High Energy Transmission Grating Spectrometer (HETGS) (Canizares et al. 2005). The HETGS has two gratings: the Medium and High Energy Gratings (MEG and HEG). The MEG has a resolution of 0.023 Å, while the HEG has a resolution of 0.012 Å, but lower sensitivity. Exposure times for the stars in our sample range from 49 to 194 ks. We used the standard reduction procedure (CIAO v3.3) for most of the spectra, but for two stars in crowded fields – HD 93129 and Cyg OB 8A – care had to be taken to properly centroid the zeroth order spectrum of the target star.

The observed spectra consist of a series of emission lines on a bremsstrahlung continuum. The lines arise from high ionization states: most lines are from helium-like or hydrogen-like ions from elements N through S, and the rest come from partially-ionized iron, primarily Fe XVII. *Chandra* is sensitive in the wavelength range from 1.2 to 31 Å. However, the shortest-wavelength line we are able to analyze in our sample stars is the Si XIV line at 6.182 Å and the shortest is the O VII line at 21.804 Å. The spectra vary in quality and some suffer from significant interstellar attenuation at longer wavelengths. These two factors determine the number of lines we are able to fit in each star.

2.2 The sample

We selected every OB star in the *Chandra* archive with a grating spectrum – see XATLAS (Westbrook et al. 2008) – that shows obviously wind-broadened emission lines, aside from ζ Pup, which we have already analyzed (Cohen et al. 2009). We eliminated from our sample those stars with known magnetic fields that are strong enough to provide significant wind confinement (this includes θ^1 Ori C and τ Sco) and we also excluded obvious colliding-wind binary X-rays, which are hard and variable (such as γ^2 Vel and η Car). δ Ori, HD 150136, and Cyg OB2-8A are possible colliding wind binary X-ray sources. They are included in the sample because their line profiles do not appear to deviate significantly from the expectations of the embedded wind shock scenario. We also exclude main sequence stars and giants with spectral type O9.5 and later, as these stars (including σ Ori AB and β Cru) have X-ray lines too narrow to be understood in the context of standard embedded wind shocks. The sample stars and their important parameters are listed in Table 1.

3 MODELING AND DATA ANALYSIS METHODOLOGY

3.1 X-ray emission line profile model

We use the model of X-ray production and absorption as described in Owocki & Cohen (2001) (OC2001). The Owocki & Cohen model has the benefit of describing a general X-ray production scenario, making few assumptions about the details of the physical mechanism that leads to the production of shock-heated plasma in the wind. The model does assume that the cold, absorbing material in the wind and the hot, X-ray-emitting material both follow a β-velocity law of the form

$$v = v_\infty(1 - \frac{\mathrm{R}_*}{r})^\beta, \quad (1)$$

where v_∞, the terminal velocity of the wind, usually has values between about 1500 and 3000 km s^{-1}. The β parameter, derived from optical and UV lines, typically has a value close to unity. The model also assumes that the volume-filling factor of X-ray emitting plasma, f, is zero below some onset radius, R_0, and follows a power law in radius of $f(r) \sim r^{-q}$ for some constant q above R_0. Our implementation of the X-ray line profile model optionally includes the effects of porosity (Owocki & Cohen 2006) and of resonance scattering (Leutenegger et al. 2007) on the individual profile shapes, but in this paper we do not include these effects in the analysis of individual profiles. We comment on the implications of this in the discussion section.

The adjustable free parameters of the profile model are generally just the normalization, the parameter that describes the onset radius of X-ray production, R_0, and a fiducial optical depth parameter, τ_*, which we describe below. For a few high signal-to-noise lines, we allow q, the power-law index of the radius-dependent filling factor, and v_∞, the terminal velocity of the wind, to be a free parameter of the fit as well. The parameter R_0, controls the width of the line via the assumed wind kinematics represented by the

Table 1. Properties of program stars.

Star	Spectral Type	$T_{\rm eff}$ (kK)	R ($R_\odot$)	log g (cm s^{-2})	v_∞ (km s^{-1})
HD 93129A	O3 If*	42.5 (5)	22.5 (5)	3.70 (5)	3200 (2)
HD 93250	O3.5 V	46.0 (5)	15.9 (5)	3.95 (5)	3250 (2)
9 Sgr	O4 V((f))	42.9 (3)	12.4 (3)	3.92 (3)	3100 (2)
HD 150136	O5 III	40.3 (3)	15.07 (3)	3.69 (3)	3400 (2)
Cyg OB2-8A	O5.5 I	38.2 (4)	27.0 (4)	3.56 (4)	2650 (4)
15 Mon	O7 V((f))	37.5 (6)	9.9 (6)	3.84 (6)	2150 (2)
ξ Per	O7.5 III(n)((f))	35.0 (5)	14.0 (5)	3.50 (5)	2450 (2)
τ CMa	O9 II	31.6 (3)	17.6 (3)	3.41 (3)	2200 (2)
ι Ori	O9 III	31.4 (4)	17.9 (4)	3.50 (4)	2350 (2)
ζ Oph	O9 V	32.0 (5)	8.9 (5)	3.65 (5)	1550 (2)
δ Ori	O9.5 II	30.6 (3)	17.7 (3)	3.38 (3)	2100 (2)
ζ Ori	O9.7 Ib	30.5 (3)	22.1 (3)	3.19 (3)	1850 (2)
ϵ Ori	B0 Ia	27.5 (1)	32.4 (1)	3.13 (1)	1600 (2)

References: (1) Searle et al. (2008); (2) Haser (1995); (3) Martins et al. (2005); (4)Puls et al. (2006); (5) Repolust et al. (2004); (6) Markova et al. (2004).

beta-velocity law. Small values of R_0 correspond to more X-ray production close to the star where the wind has a low Doppler shift, while large values of R_0 indicate that most of the X-rays come from high Doppler shift regions in the outer wind. Hydrodynamic models show shocks developing about half a stellar radius above the surface of the star – albeit with some variation based on treatments of the line force parameters and of the lower boundary conditions in the numerical simulations (Feldmeier et al. 1997; Runacres & Owocki 2002) – so we should expect R_0 to be about 1.5 R_*.

The optical depth of the wind affects the blue shift and asymmetry of the line profile. The optical depth at a given location in the wind, and thus at a given wavelength, is proportional to the constant τ_*, given by

$$\tau_* = \frac{\kappa \dot{M}}{4\pi R_* v_\infty}. \quad (2)$$

This constant appears in the exact expression for the optical depth at any arbitrary point in the wind,

$$\tau(p,z) = \int_z^\infty \kappa\rho(r')dz' = \tau_* \int_z^\infty \frac{R_* dz'}{r'^2(1-R_*/r')^\beta}, \quad (3)$$

where p, z are the usual cylindrical coordinates: the impact parameter, p, is the projected distance from the z-axis centered on the star and pointing toward the observer, and $r \equiv \sqrt{p^2+z^2}$. The second equality arises from substituting the beta-velocity law into the general equation for the optical depth and employing the mass continuity equation. The value of τ_* controls the degree of asymmetry and blue shift of each line profile. The profile is calculated from

$$L_\lambda \propto \int_{R_0}^\infty \eta e^{-\tau} dV, \quad (4)$$

where η is the X-ray emissivity, τ is calculated using eq. 3, and the volume integral is performed over the entire wind above $r = R_0$. In addition to scaling with the mass-loss rate, τ_* is proportional to κ, the atomic opacity, and is thus dependent on wavelength. Note that the atomic opacity is constant across a given line profile but it varies from line to line.

3.2 Fitting procedure

All model fitting was done in XSPEC (v12.3). We fit the positive and negative first order spectra simultaneously, but not coadded. Coadded spectra are shown in the figures for display purposes, however. When there were a significant number of counts in the HEG measurements of a given line, we included those data in the simultaneous fits. In most cases, there were negligible counts in the HEG data and we fit only the MEG data. Because Poisson noise dominates these low-count *Chandra* data, we could not use χ^2 as the fit statistic, and instead used the C statistic (Cash 1979). As with χ^2, a lower C value indicates a better fit, given the same number of degrees of freedom. We assessed goodness-of-fit via Monte Carlo simulations of the distribution of the C statistic for each line fit. For placing confidence limits on model parameters, ΔC is equivalent to $\Delta\chi^2$, with a ΔC value of 1 corresponding to a 68% confidence bound in one dimension (Press et al. 2007). We establish confidence bounds on the model parameters of interest one at a time, allowing other

parameters to vary while establishing these bounds. There is generally a mild anti-correlation between R_0 and τ_*, so it is useful to evaluate the joint constraints on two parameters, adjusting the corresponding value of ΔC accordingly. Joint confidence limits are shown for fits to the Fe XVII line at 15.014 Å for several sources in Fig 1.

To account for the weak continuum under each emission line, we first fit a region around the line with a continuum model having a constant flux per unit wavelength. This continuum model was added to the line-profile model when fitting the line itself. The fitting was generally then done with three free parameters: τ_*, R_0, and a normalization factor. We fixed β at 1, q at 0, and v_∞ at the value given in Table 1[1]. A discussion of the effects of changing β, q, and v_∞ as well as sensitivity to continuum placement, treatment of blends, and other aspects of our analysis can be found in Cohen et al. (2009).

The hydrogen-like lines in the spectra consist of two blended lines with wavelength separations that are much smaller than the resolution of the *Chandra* gratings. We fit these lines with a single model centered at the emissivity-weighted average of the two wavelengths. In some cases, the hydrogen-like lines or the strong iron lines are blended with weaker lines. If the blending is too severe to be modeled, as it is for the O VIII Lyman-β line at 16.006 Å, we excluded the line from our analysis entirely. If the blended portion of the line could be omitted from the fit range without producing unconstrained[2] results, we simply fit the model over a restricted wavelength range. The Ne X line at 12.134 Å, for example, produces well-constrained results, even when its red wing is omitted due to blending. If lines from the same ion are blended, such as the Fe XVII lines at 16.780, 17.051, and 17.096 Å, we fit three models to the data simultaneously, constraining the τ_* and R_0 values to be the same for all lines. In the case of the aforementioned iron complex, we also constrained the ratio of the normalizations of the two lines at 17.096 and 17.051 Å, which share a common lower level, to the theoretically predicted value of 0.9 because the blending is so severe.

The helium-like complexes are among the strongest lines in many of the sample stars' spectra, but they are generally heavily blended. The line intensity ratios are a function of the local mean intensity of the UV radiation at the location of the X-ray emitting plasma. And so the spatial (and thus velocity) distribution of the shock-heated plasma affects both the line intensity ratios and the line profile shapes. We model these effects in tandem and fit all three line profiles, including the relative line intensities, simultaneously, as described in Leutenegger et al. (2006). In order to do this, we use UV fluxes taken from TLUSTY (Lanz & Hubeny 2003) model atmospheres appropriate for each star's effective temperature and $\log g$ values, as listed in Table 1. This procedure generates a single τ_* value for the entire complex.

[1] For ζ Ori, a terminal velocity of 1860 km s^{-1} was used instead of the 1850 km s^{-1} in Haser (1995) for comparison to the results of Kramer, Cohen, & Owocki (2003)

[2] Unconstrained in the sense that the ΔC criterion does not rule out significant portions of model parameter space.

3.3 Analyzing the ensemble of line fits from each star

To extract the mass-loss rate from a single derived τ_* parameter value, a model of the opacity of the cold, unshocked component of the wind is needed. Then, along with values for the wind terminal velocity and stellar radius, Eq. 2 can be used to derive a mass-loss rate for a given line. To derive a single mass-loss rate from an ensemble of emission lines, each with their own τ_* value, as we do here, the wavelength dependence of the τ_* values is assumed to share the wavelength dependence of the atomic opacity, and Eq. 2 is solved for the best $\tau_*(\lambda)$. Although this trend was not noted in the initial analyses of *Chandra* grating spectra, it has recently been shown for ζ Pup that if all lines in the spectrum are considered and a realistic model of the wavelength-dependent wind opacity is used, then the wavelength trend in the ensemble of τ_* values is consistent with the atomic opacity (Cohen et al. 2009).

The opacity of the bulk wind is due to bound-free absorption (inner shell photoionization), and the contributions from N, O, and Fe are dominant, with important contributions from Ne and Mg at wavelengths below about 12 Å. The wind opacity is affected by the elemental abundances – both the overall metallicity and also the relative contributions of specific elements, most notably N and O, which are altered by CNO processing – and, to a lesser extent, by the ionization distribution in the wind. In general, there do not exist precise abundance determinations for most of the stars in our sample. The expectation is that these massive stars have metallicities close to solar, and that some, but not all, have enhanced nitrogen and depleted carbon and oxygen. Thus, we have calculated two generic wind opacity models: one using solar (Asplund, Grevesse, & Sauval 2005) abundances and one that uses overall solar metallicity but has N at ten times solar, O at 0.4 solar and C at 0.06 solar. We refer to these as the "solar" and "CNO processed" wind opacity models. Both assume an ionization balance based on O star models in MacFarlane, Cohen, & Wang (1994), but the opacity is largely insensitive to reasonable changes in the ionization distribution. We show these two opacity models in Fig. 2. Note that from 5 to 20 Å, the two models are similar, with the solar model having a slightly higher opacity. At 20 Å, however, the oxygen K-shell edge is more apparent in the solar model than in the CNO processed model. The only line that we are able to model past the oxygen edge is the O VII line complex at 21.7 Å. This line is not strong in any of our sources, but with higher-resolution data, it could be possible to use it to differentiate between the two opacity models.

4 RESULTS

In almost all cases, the OC2001 model provides statistically good fits to individual lines. The one exception is δ Ori, for which the best fit is ruled out at the 99% level for several lines. There appears to be a slight red shift in δ Ori's spectrum, suggesting a small systematic error in the wavelength scale. Adding a shift parameter to the model improved the fit significantly, and the results obtained from these fits are the ones we present here.

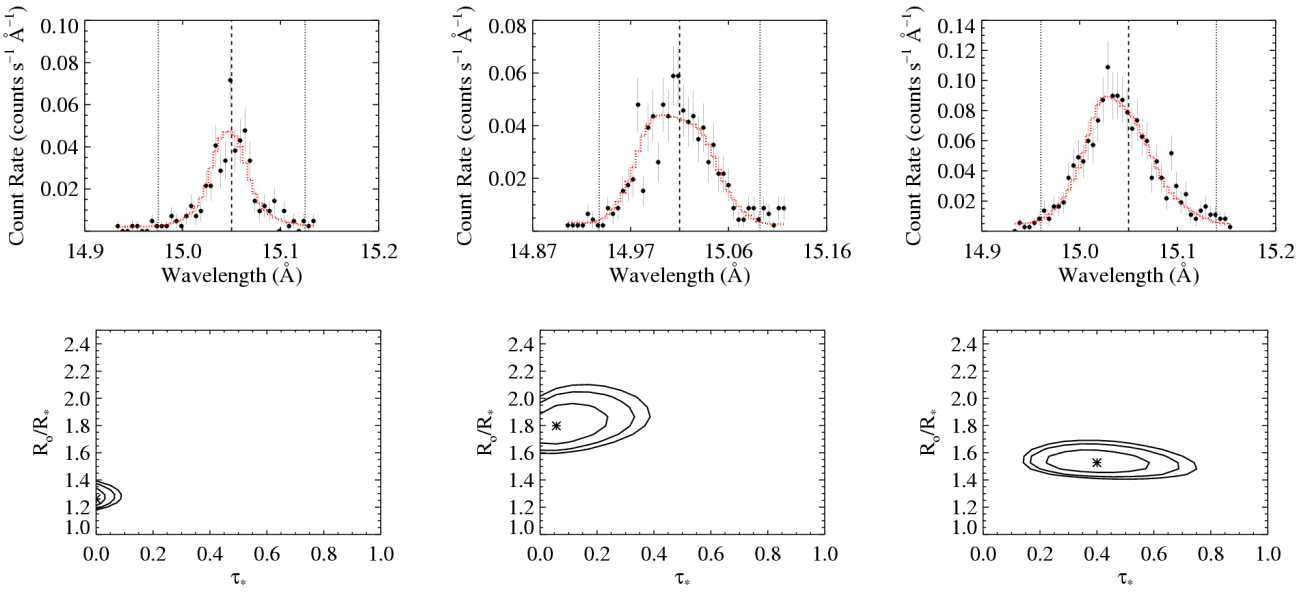

(a) ζ Oph: $\tau_* = 0.0\,^{+0.013}_{-0.0}$. (b) ϵ Ori: $\tau_* = 0.064\,^{+0.101}_{-0.064}$. (c) ζ Ori: $\tau_* = 0.379\,^{+0.132}_{-0.111}$.

Figure 1. The Fe XVII line at 15.014 Å with best-fit model and two-dimensional parameter constraints for several sources, showing various degrees of asymmetry. The errors on τ_* represent a 68% one-dimensional confidence interval, and contours give the 68%, 90%, and 95% two-dimensional confidence limits. The vertical dashed lines on the profile plots represent the laboratory line centroid and the wavelengths corresponding to the terminal velocity of the wind.

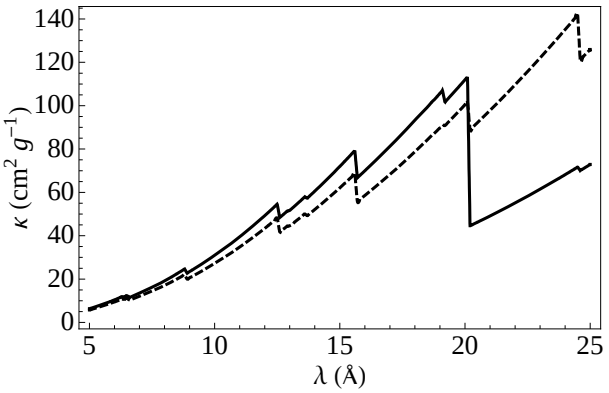

Figure 2. The two models of the opacity, $\kappa(\lambda)$ (cm^2 g^{-1}). Both assume the same overall solar metallicity (Asplund, Grevesse, & Sauval 2005) but the model with the dashed line has N enhanced by a factor of 5 and O and C by factors of 0.1.

For most of the stars, a wavelength dependence of the fitted τ_* values is evident, while for other stars, especially ζ Oph and ϵ Ori, there is no obvious wavelength trend, although the relatively noisy τ_* data are generally consistent with the wavelength dependence expected from detailed models of the wind opacity. The τ_* and mass-loss rate results are shown in Fig. 3 and summarized in Tab. 2. By fitting the τ_* ensembles, we obtain mass-loss rates between 2×10^{-9} M$_\odot$ yr^{-1} for ζ Oph and 8.53×10^{-6} M$_\odot$ yr^{-1} for HD 93129A. As expected, the X-ray mass-loss rates are lower than the corresponding literature values. For HD 93129A, 9 Sgr, and ξ Per, we find a reduction by a factor of 3-5. For HD 93250, Cyg OB2-8A, δ Ori, ζ Ori, and ϵ Ori, mass-loss rates are reduced by an order of magnitude, and for τ CMa and ζ Oph, they are reduced by almost two orders of magnitude. Note, however, that the comparison mass-loss rate for ζ Oph is an upper limit, so the actual revision may be less drastic.

The errors presented in Tab. 2 represent only the error associated with fitting the data using a weighted least-squares regression. Other factors may also contribute to error in our derived mass-loss rates. The uncertainties in the opacity model have already been discussed in § 3.3. As new information comes to light about potential non-solar metallicities, it can be incorporated into our mass-loss rate results by simply scaling the opacity by the metallicity and the mass-loss rate will change by a corresponding (but opposite) amount. Additionally, the stars' radii and terminal velocities all have associated uncertainties that are not taken into account by our fitting procedure. As τ_* is inversely proportional to R$_*$, our mass-loss rate values can be adjusted for updated stellar radii by simply scaling the mass-loss rate by the same factor as the radius. The dependence of τ_* on v_∞ is more complex. A detailed description of the effects that changing the terminal velocity has on mass-loss rate determination can be found in Cohen et al. (2009).

The shock onset radius that we obtained for each star is, in general, consistent with formation of shocks at 1.5 R$_*$, as predicted by the hydrodynamic models of Feldmeier et al. (1997) and Runacres & Owocki (2002). The R_0 values for each star are shown in Fig. 4, and the average values are listed in Tab. 2. In some of the R_0 spectra, a slight positive trend with wavelength is apparent. However, the null hypothesis of 0 slope is ruled out only in the cases of δ Ori and ϵ Ori, with p-values of 0.0239 and 0.0107, respectively.

For stars with high signal to noise spectra, we were able to determine X-ray terminal velocities, as shown in Fig. 5.

Table 3. Derived terminal velocities.

Star	Spectral Type	v_∞ (km s^{-1})	X-ray v_∞ (km s^{-1})
9 Sgr	O4 V	3100	2692^{+197}_{-197}
HD 150136	O5 III	3400	3024^{+173}_{-197}
ξ Per	O7.5 III	2450	2610^{+169}_{-168}
ζ Oph	O9 V	1550	1386^{+122}_{-120}
δ Ori	O9.5 II	2100	2330^{+132}_{-130}
ζ Ori	O9.7 I	1850	1883^{+50}_{-49}
ϵ Ori	B0 I	1600	1728^{+97}_{-97}

The velocities we obtain differ from the values presented by Haser (1995) by less than 15%. We find terminal velocities lower than Haser's values for 9 Sgr, HD 150136, and ζ Oph, and velocities higher than Haser's values for ξ Per, δ Ori, ζ Ori, and ϵ Ori. These results are summarized in Tab. 3.

5 DISCUSSION AND CONCLUSIONS

We have systematically confirmed and quantified the lack of strong wind absorption effects in *Chandra* grating observations of O-star X-ray line profiles. Assuming that the profile shapes are dominated by the atomic opacity in a non-porous wind, we derive mass-loss rates that vary from being marginally lower than the traditional mass-loss rate to being more than an order of magnitude lower. For HD 93129A, 9 Sgr, and ξ Per, we find mass-loss rate reductions that are comparable to those indicated by other diagnostics when small-scale clumping is taken into account. Reductions by one or two orders of magnitude, however, are not seen in clumping reanalysis. An order of magnitude reduction is difficult to accept, but it is conceivable for some of the sample stars, given the weakness of UV absorption lines in their spectra. τ CMa exhibits the largest mass-loss rate revision of almost a factor of 100. This star's spectrum is very weak, and we were able to fit only three lines. Given the uncertainties in its mass-loss rate, a reduction by an order of magnitude is not ruled out.

Previous works (Kramer, Cohen, & Owocki 2003; Cohen et al. 2006; Oskinova et al. 2006) have claimed to see no wavelength trend in τ_* values. In particular, Cohen et al. (2006) presents τ_* values for ζ Ori that appear to be randomly distributed. However, results are only shown for lines above 12 Å. We find that most of the leverage for the wavelength trend comes from lines below 10 Å, and that this is the case for ζ Ori.

Porosity has been invoked to explain the lack of strong wind absorption in X-ray line profiles. Indeed, porosity would flatten out the effective opacity and decrease τ_* values without having to reduce the mass-loss rate. However, it is unlikely that porosity can completely explain our order-of-magnitude mass-loss rate reductions. All of the stars with moderate mass-loss rate reductions are of spectral type O7.5 or earlier, while the later-type stars tend to have mass-loss rates of an order of magnitude or more. The fact that many of the biggest and hardest to accept mass-loss rate reductions are for late-O and early-B stars that have the lowest mass-loss rates makes it unlikely that significant wind porosity effects are causing the relative lack of asymmetry in the observed X-ray line profiles. Porosity requires individual clumps to be optically thick to X-rays. For the later-type OB stars in our sample, the entire wind has negligible optical depth, so the level of clumping needed to generate significant porosity would be extreme.

In fitting the data, we assumed that the shocked regions of the wind follow the same beta velocity law as the bulk wind. If, however, the shocked plasma has a lower terminal velocity than the surrounding wind, then the terminal velocities we used to fit the data would be too high, and the τ_* values we derived would consequently be lower than their real values. However, when we fit terminal velocities to the X-ray lines, we obtain values that are in general consistent with the bulk wind velocities, with some of the X-ray values being higher and some lower than the bulk wind values. There is thus no evidence for the X-ray terminal velocities being systematically lower than the velocities of the absorbing material.

In addition to quantifying the lack of absorption in X-ray line profiles, we are also able to constrain the location of X-ray emitting material by deriving shock onset radii. The R_0 values we obtain from the X-ray line profiles confirm the prediction of hydrodynamic simulations by Feldmeier et al. (1997) and Runacres & Owocki (2002) that shocks should begin forming about 0.5 R$_*$ above the surface of the star. For δ Ori and ζ Oph, R_0 is only a few tenths of a stellar radius above the surface of the star, but such values are reasonable given the adjustable parameters on the hydrodynamic simulations. The wavelength trend that we find in R_0 values is unexpected but not inexplicable. A positive wavelength dependence in R_0 could imply that shock regions with the high temperatures needed to produce H-like and He-like Si and Mg are located closer to the star than the cooler regions where highly-ionized O is formed.

In general, our results are consistent with the wind shock paradigm. The OC2001 model provides a good fit to the X-ray line profiles, indicating that line-widths are consistent with Doppler broadening in the wind. The R_0 values we derive match predictions of hydrodynamic models of shock formation, and the terminal velocities we obtain for X-ray emitting material are consistent with the terminal velocities of the bulk wind. We also see evidence of the attenuation of X-rays by the bulk wind in the asymmetric shape of individual line profiles and in the overall trend of asymmetry vs. wavelength. As has previously been noted, in both cases, the effects of absorption are not as strong as expected given mass-loss rates obtained from Hα, UV, and radio diagnostics. We have quantified this lack of absorption for the first time. Our results indicate that deriving mass-loss rates from X-ray line profiles is a promising technique, but that for some massive stars, it is not clear that the large mass-loss rate reductions derived this way can be taken at face value.

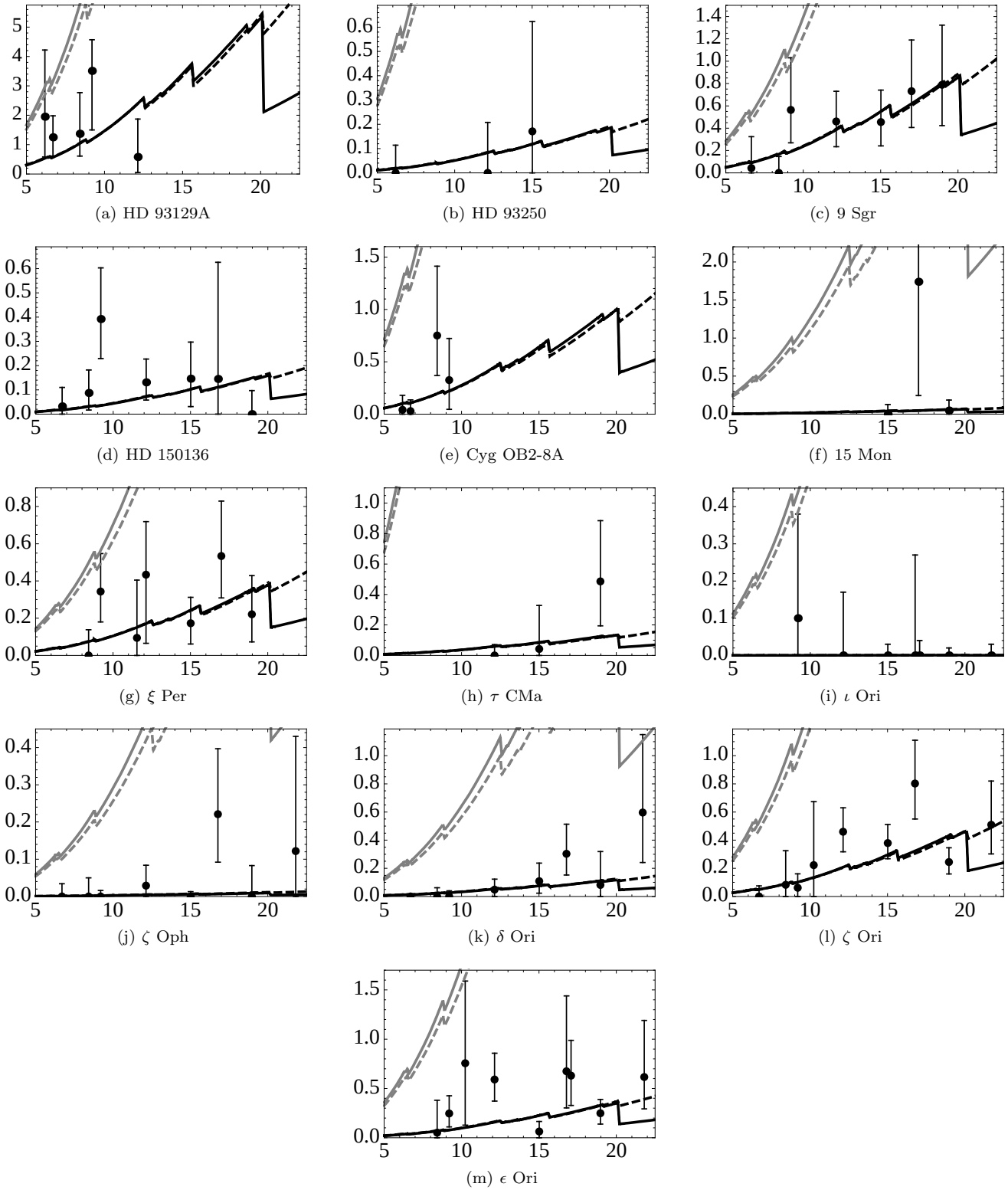

(a) HD 93129A (b) HD 93250 (c) 9 Sgr

(d) HD 150136 (e) Cyg OB2-8A (f) 15 Mon

(g) ξ Per (h) τ CMa (i) ι Ori

(j) ζ Oph (k) δ Ori (l) ζ Ori

(m) ϵ Ori

Figure 3. τ_*values vs. wavelength and corresponding mass-loss rate fits for the 10 stars in our sample. Error bars represent the 68% confidence limits. Literature mass-loss rates are shown in gray. The solar opacity model is shown with a solid line, and the CNO processed model with a dashed one.

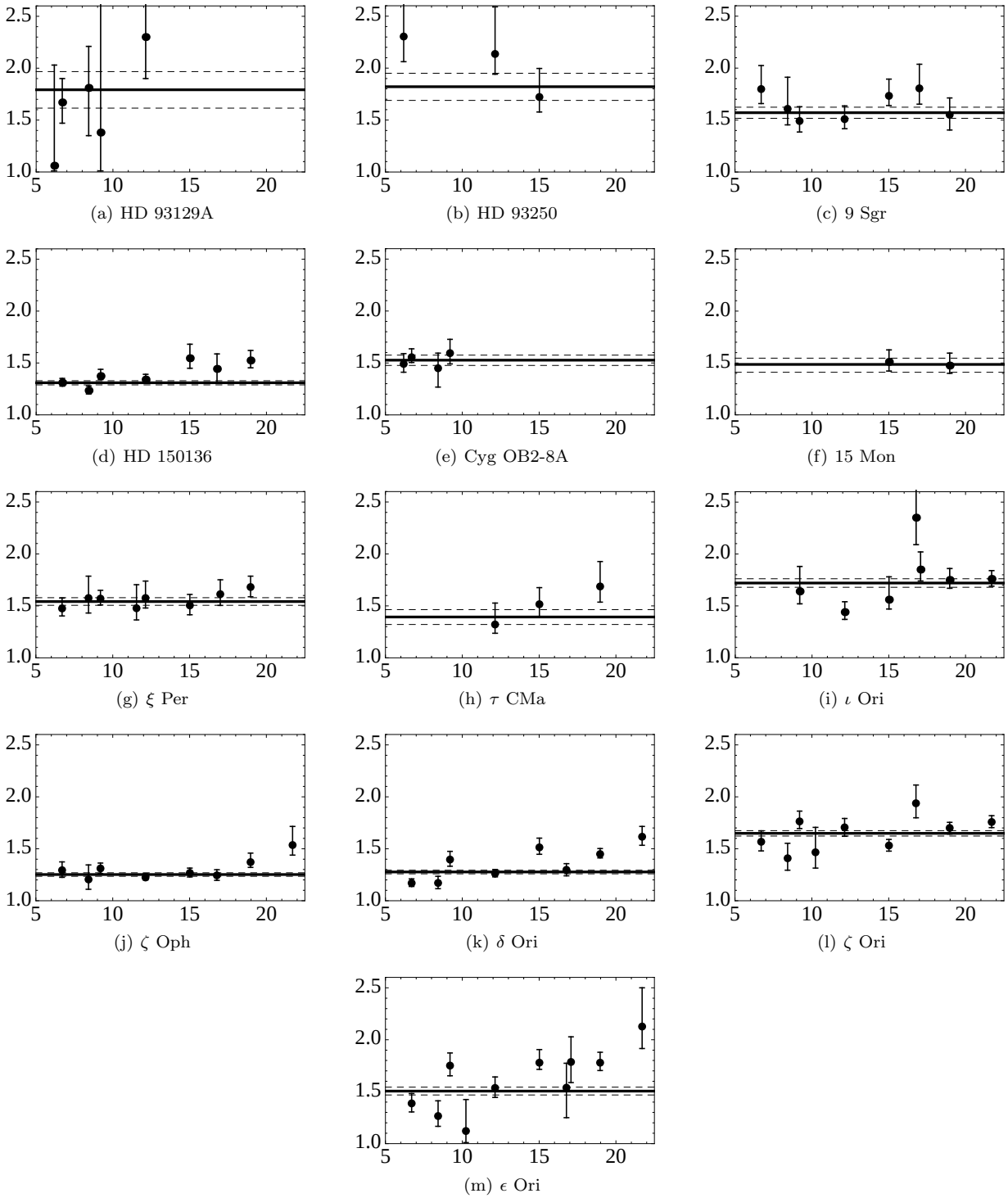

Figure 4. Derived R_0 values for each line in each star, plotted vs. wavelength.

REFERENCES

Asplund M., Grevesse N., Sauval A. J., 2005, in Bash F. N., Barnes T. G., eds, Cosmic Abundances as Records of Stellar Evolution and Nucleosynthesis. Astron. Soc. Pac., San Francisco, p. 25

Bouret J.–C., Lanz T., Hillier D. J., 2005, A&A, 438, 301

Canizares C. R., et al., 2005, PASP, 117, 1144

Cash W., 1979, ApJ, 228, 939

Cassinelli J. P., Miller N. A., Waldron W. L., MacFarlane J. J., Cohen D. H., 2001, ApJ, 554, L55

Cohen D. H., Leutenegger M. A., Grizzard K. T., Reed C. L., Kramer R. H., Owocki S. P., 2006, MNRAS, 368, 1905

Cohen D. H., Leutenegger M. A., Townsend R. H. D., 2008, in Hamann W.–R., Feldmeier A., Oskinova L. M., eds, Clumping in Hot Star Winds. Universitatsverlag, Potsdam, p. 209

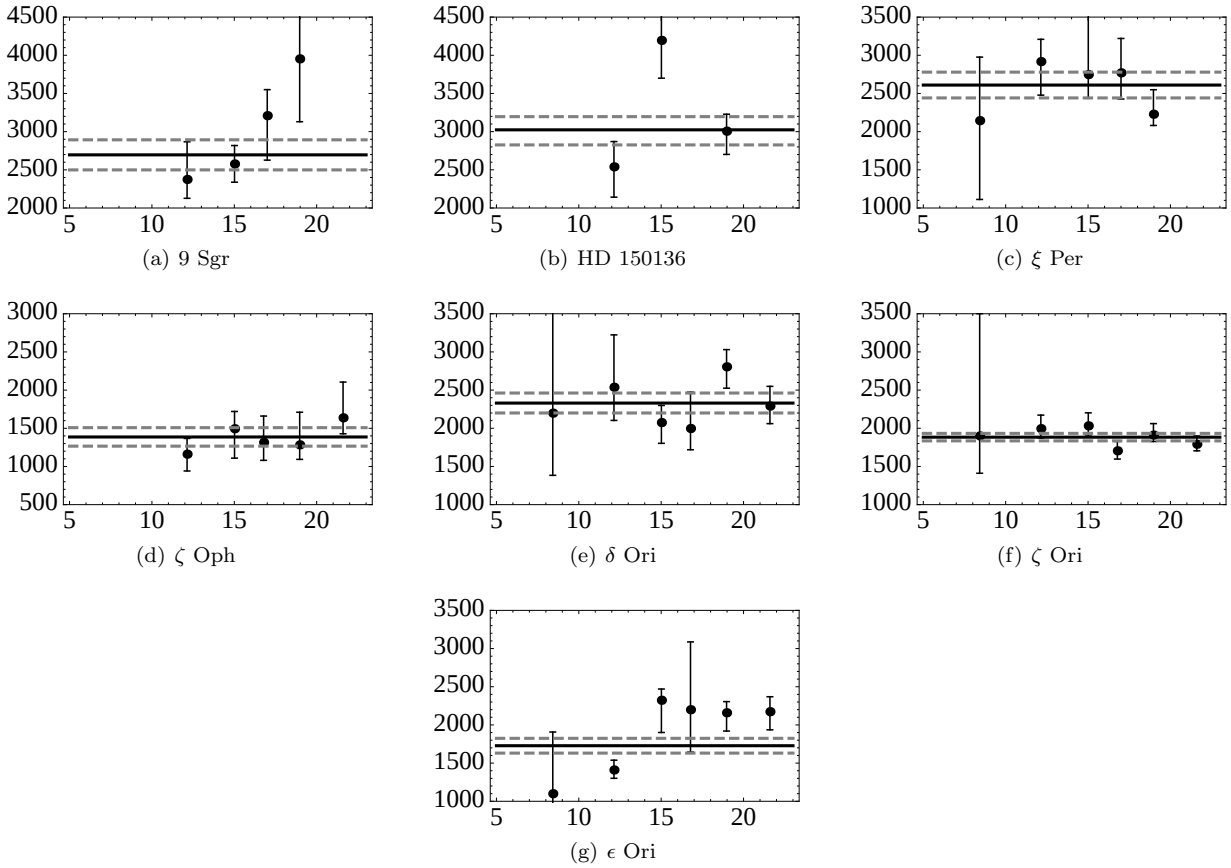

(a) 9 Sgr (b) HD 150136 (c) ξ Per

(d) ζ Oph (e) δ Ori (f) ζ Ori

(g) ϵ Ori

Figure 5. Derived v_∞ values plotted vs. wavelength.

Table 2. Derived properties of program stars. Errors represent a 68% confidence interval.

Star	Spectral Type	Literature $\dot{M}$ (10^{-6} $M_\odot$ yr^{-1})	X-ray $\dot{M}$ (Solar opacity) (10^{-6} $M_\odot$ yr^{-1})	X-ray $\dot{M}$ (CNO opacity) (10^{-6} $M_\odot$ yr^{-1})	R_0 (R_*)
HD 93129A	O3 I	26.3 (1)	$4.73^{+1.85}_{-1.84}$	$5.37^{+2.09}_{-2.08}$	$1.79^{+0.18}_{-0.18}$
HD 93250	O3.5 V	3.45 (1)	$0.118^{+0.182}_{-0.118}$	$0.137^{+0.205}_{-0.137}$	$1.82^{+0.13}_{-0.15}$
9 Sgr	O4 V	2.4 (2)	$0.407^{+0.108}_{-0.100}$	$0.471^{+0.124}_{-0.115}$	$1.57^{+0.05}_{-0.06}$
HD 150136	O5 III		$0.083^{+0.038}_{-0.037}$	$0.097^{+0.044}_{-0.042}$	$1.31^{+0.02}_{-0.02}$
Cyg OB2-8A	O5.5 I	11.2 (3)	$0.885^{+0.572}_{-0.564}$	$0.988^{+0.640}_{-0.633}$	$1.52^{+0.04}_{-0.05}$
15 Mon	O7 V	1.2 (4)	$0.017^{+0.30}_{-0.017}$	$0.020^{+0.035}_{-0.020}$	$1.49^{+0.06}_{-0.08}$
ξ Per	O7.5 III	1.08 (1)	$0.161^{+0.054}_{-0.050}$	$0.184^{+0.070}_{-0.059}$	$1.54^{+0.04}_{-0.03}$
τ CMa	O9 II	6.31 (2)	$0.064^{+0.058}_{-0.056}$	$0.072^{+0.067}_{-0.062}$	$1.39^{+0.07}_{-0.07}$
ι Ori	O9 III	1.03 (3)	$0.0004^{+0.0091}_{-0.0004}$	$0.0003^{+0.0092}_{-0.0003}$	$1.72^{+0.04}_{-0.04}$
ζ Oph	O9 V	≤ 0.18 (1)	$0.002^{+0.003}_{-0.002}$	$0.002^{+0.003}_{-0.002}$	$1.25^{+0.02}_{-0.02}$
δ Ori	O9.5 II	1.07 (2)	$0.054^{+0.029}_{-0.028}$	$0.064^{+0.032}_{-0.032}$	$1.28^{+0.02}_{-0.02}$
ζ Ori	O9.7 I	2.51 (2)	$0.234^{+0.041}_{-0.041}$	$0.264^{+0.046}_{-0.046}$	$1.65^{+0.02}_{-0.03}$
ϵ Ori	B0 I	4.07 (2)	$0.225^{+0.061}_{-0.063}$	$0.262^{+0.070}_{-0.067}$	$1.51^{+0.03}_{-0.04}$

Literature mass-loss rates do not take clumping and density-squared effects into account, but radio determinations are used whenever possible in order to attempt to minimize the effects of clumping. References: (1) Repolust et al. (2004); (2) Lamers & Leitherer (1993); (3) Puls et al. (2006); (4) Markova et al. (2004).

Cohen D. H., Leutenegger M. A., Wollman E. E., Zsargó J., Hillier D. J., Townsend R. H. D., Owocki S. P., 2009, MNRAS, submitted
Feldmeier A., Puls J., Pauldrach A. W. A., 1997, A&A, 322, 878
Fullerton A. W., Massa D. L., Prinja R. K., 2006, ApJ, 637, 1025
Haser S. M., 1995, Ph.D. Thesis, Univ. Munich
Kahn S. M., Leutenegger M. A., Cottam J., Rauw G., Vreux J.–M., den Boggende A. J. F., Mewe R., Güdel M., 2001, A&A, 365, L312
Kramer R. H., Cohen D. H., Owocki S. P., 2003, ApJ, 592, 532
Lanz T., Hubeny I., 2003, ApJS, 146, 417
Lamers H. J. G. L. M., Leitherer C., 1993, ApJ, 412, 771
Leutenegger M. A., Owocki S. P., Paerels F. B. S., Kahn S. M., 2007, ApJ, 659, 642
Leutenegger M. A., Paerels F. B. S., Kahn S. M., Cohen D. H., 2006, ApJ, 650, 1096
MacFarlane J. J., Cohen D. H., Wang P., 1994, ApJ, 437, 351
Markova N., Puls J., Repolust T., Markov H., 2004, A&A, 413, 693
Martins F., Schaerer D., Hillier D. J., 2005, A&A, 436, 1049
Oskinova L., Feldmeier A., Hamann W.–R., 2006, MNRAS, 372, 313
Owocki S.P., Cohen D. H., 2001, ApJ, 559, 1108
Owocki S. P., Cohen D. H., 2006, ApJ, 648, 565
Press W. H., Flannery B. P., Teukolsky S. A., Vetterling W. T., 2007, Numerical Recipes, 3^{rd} edition. Cambridge University Press, Cambridge
Puls J., Kudritzki R. P., Herrero A., Pauldrach A. W. A., Haser S. M., Lennon D. J., Gabler R., Voels S. A., Vilchez J.M., Wachter S., Feldmeier A., 1996, A&A, 305, 171
Puls J., Markova N., Scuderi S., Stanghellini C., Taranova O. G., Burnley A. W., Howarth I. D., 2006, A&A, 454, 625
Repolust T., Puls J., Herrero A., 2004, A&A, 415, 349
Runacres M. C., Owocki S.P., 2002, A&A, 381, 1015
Searle D. C., Prinja R. K., Massa D., Ryans R., 2008, A&A, 481, 777
Westbrook, O. W., et al., 2008, ApJS, 176, 218
Zhekov07